Mechanism and Machine Theory 76 (2014) 56–69

Contents lists available at ScienceDirect

Mechanism and Machine Theory

journal homepage: www.elsevier.com/locate/mechmt

Inverse kinematics and workspace analysis of a cable-driven parallel robot with a spring spine

Bingtuan Gao [a,*], Honggang Song [b], Jianguo Zhao [c], Shaoxiong Guo [a], Lixia Sun [b], Yi Tang [a]

[a] School of Electrical Engineering, Southeast University, Nanjing, China
[b] College of Energy and Electrical Engineering, Hohai University, Nanjing, China
[c] Department of Electrical and Computer Engineering, Michigan State University, East Lansing, USA

ARTICLE INFO

Article history:
Received 21 July 2013
Received in revised form 27 January 2014
Accepted 30 January 2014
Available online 2 March 2014

Keywords:
Cable-driven
Parallel robot
Kinematics
Workspace
Optimal design

ABSTRACT

We present a cable-driven flexible parallel robot with low motion noise to mimic a human neck in this paper. The fixed base and moving platform of the robot are connected by three cables and a compression spring. The spring serves as the cervical spine to support and facilitate the motion of moving platform corresponding to human head. The cables serve as the muscles around the human neck to drive the robot. Due to the flexible compression spring, we cannot solve the inverse kinematics directly. As shown in this paper, it should be combined with the statics for possible solutions. Based on the inverse kinematics and statics analysis, we optimize the cable placements to minimize the actuation force. Moreover, the workspace of the robot is analyzed with the constraint of positive cable tension. Simulations were performed and demonstrated the correctness and feasibility of the inverse kinematics and workspace analysis of the parallel robot. The approach presented in this paper can be extended to other parallel robots with a flexible compression spring.

1. Introduction

In harmful environments where there exist nuclear radiations or chemical substances, people need to wear personal protective equipments such as donning respirators or chemical-resistant jackets. But these personal protective equipments will generate noises when users move around. The noises generated by moving the head are extremely harmful because they may influence people's hearing of useful information and make them perform wrong actions. Therefore, we should analyze the effect of such noises on a human's hearing. To conduct such an acoustic investigation, we can use a low motion noise robotic neck for experiments instead of relying on humans to perform head movements which may cost higher and not achieve the ideal results [1].

To successfully use a robotic neck for such acoustic experiments, it should resemble a human neck in two key ways. On one hand, it should have the same degree of freedom and motion range as a human. This way, we can conduct the experiment for various types of motion and motion ranges. On the other hand, the robotic neck should not make noises itself during the movements without wearing equipments such as respirators or jackets. To examine the noise effect of wearing equipment, all the other noises should be eliminated as much as possible.

The principles of human head movements have been studied extensively in the biomechanics field. Clinical studies show that the head motion relies on the cervical portion of the human spine consisting of seven cervical vertebrae [2]. Although each vertebra has 6 DOF (degree of freedom), researchers usually take the overall neck as 3DOF (pitch, roll, and yaw). Many humanoid neck mechanisms in the context of humanoid robots have been designed and developed in the past decade. We divide all of them into two categories: serial and parallel. The serial neck has advantages of simple structures and easy control because each DOF of

* Corresponding author. Tel.: +86 25 83794163; fax: +86 25 83790617.
E-mail address: gaobingtuan@seu.edu.cn (B. Gao).

0094-114X/$ – see front matter © 2014 Elsevier Ltd. All rights reserved.
http://dx.doi.org/10.1016/j.mechmachtheory.2014.01.016

the neck is actuated independently. The Honda ASIMO [3] and HRP-2 [4] have serial necks with two DOF—pitch and roll. The Dav [5], the Albert HUBO [6], and the final design of iCub [7] have serial necks with three DOF—pitch, roll, and yaw. The robots presented in [8,9] have serial necks with four DOF in which an additional nodding DOF is considered. The parallel neck is based on a parallel manipulator, which consists of a moving platform, a fixed base, several identical actuated chains, and a passive spine if necessary [10]. This approach normally realizes the two DOF of the neck motion, i.e. pitch and roll, and the yaw motion is accomplished by an additional mechanism. The head mechanism of SAYA is based on a spring spine and several pneumatic artificial muscles [11]. The iCub robot has two parallel necks in addition to the serial one. The first one uses a spring spine and three actuated cables; the second one uses a three DOF parallel manipulator with a central passive spherical strut [12]. The James [13] humanoid robot also has a head similar to the first parallel neck of iCub. Another parallel neck mechanism based on two cable-driven elastic limbs and a passive limb without a spine is proposed in [14].

Although all the robotic necks in the previous papers can realize the head motion, they fail to achieve the low-motion noise as the actuators are installed inside the robot. An exception is the acoustical telepresence robot presented in [15], which can reconstruct the sound environment for a listener at a remote location and follow the listener's head motion at the same time. The robot is driven by motors via cable and pulley systems. Since no gears are used in the robot, the noise from the robot motion can be low. Nevertheless, the motors can still generate considerable noise since they are installed right beneath the head. The same group also investigated the feasibility of using the ultrasonic servomotor to replace the traditional motor [16].

To eliminate the movement noise, we propose a mechanism shown in Fig. 1. Its key mechanism is a cable-driven parallel manipulator with a spring spine, which has a similar function of the cervical vertebrae in human necks. It supports the robotic head and can bend around the neutral axis to generate two DOF pitch and roll movements. A cable–pulley structure mounted on the moving platform is used to realize the yaw motion. Three driving cables, with similar functions of human neck muscles, are equally spaced at 120° on both the moving platform and the base. The pitch and roll motion of the moving platform is driven by these three cables, which are remotely pulled by the actuators sealed in a sound insulation box. Between the robotic head and the sound insulation box, the driving cables are guided and protected by cable housings. As no sound generation parts are embedded into the robotic neck, little noise is generated by the robotic neck during its motions.

The mechanism shown in Fig. 1 belongs to the general cable-driven parallel mechanisms, which has recently attracted many research interests. Compared to traditional mechanisms, cable-driven parallel mechanisms have the advantages of large workspace, low inertia, high payload to weight ratio, transportability, reconfigurability, and full remote actuation [17]. As a result, cable-driven mechanisms are well-suited for applications such as surveillance of large-scale places, interaction with disaster sites, and manipulation of heavy payloads. Since cables can only generate unilateral pulling force, the full control of cable-driven parallel mechanisms with n DOF needs at least $n + 1$ cables. For mechanisms with cable numbers no more than the number of DOF, extra loads or wrenches are required to determine the pose of the moving platform together with the driving cables. Some researches call these cable-driven parallel mechanisms as underconstrained cable-driven parallel mechanisms [18–20]. The mechanism considered in this paper, as shown in Fig. 1, is a typical underconstrained cable-driven parallel mechanism because only three cables are used to control three DOF of the moving platform, i.e., its height, pitch angle, and roll angle, which leads to the challenge of dealing with the coupling between the kinematics and the statics.

A large number of cable-driven mechanisms have been developed, such as the RoboCrane for moving heavy loads over a large workspace [21], the WARP manipulator for high-speed assembly of lightweight objects [22], the large-scale FAST system for a large radio telescope receiver [23], the NIMS3D cabled robot for actuated sensing applications [24], and the flexible link mechanism for keeping stiffness against load [25]. There are also many studies on kinematics, workspace, and optimal cable

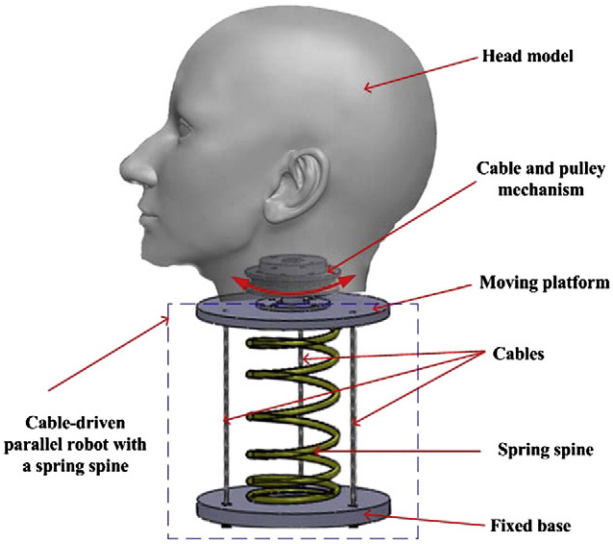

Fig. 1. Overview of the parallel robotic neck design.

tension distribution for cable-driven parallel mechanisms. A path-planning method was developed for cable-driven robot and the kinematics and statics are analyzed in [26]. With a closed-loop vector method and a geometric methodology, inverse kinematics of a hybrid-driven cable-suspended parallel robot with three translational DOF for singularity analysis was performed in [27]. Based on the force-closure condition, the force-closure workspace of a cable-driven parallel mechanism was obtained in [28]. In [29], the wrench-closure workspace (WCW) was studied and the poses of the WCW are characterized. Optimal cable tension distribution for a cable-driven parallel manipulator was studied by a projection method in [30].

Although there exist many researches on cable-driven mechanisms, little research adequately analyzes a cable-driven robotic neck with a spring spine. In [10], we have proposed a flexible humanoid neck system driven by four cables and analyzed the inverse kinematics and statics in detail. However, four cables create a redundancy to realize the pitch and roll motion of the moving platform which increases the cost of the system. Theoretically, only three cables are needed to realize the two DOF pitch and roll motion. In other words, parallel mechanisms driven by three cables are the basic configuration for multi-cables driven humanoid neck parallel mechanism. Therefore, its inverse kinematics and statics is studied extensively in this paper. Based on the kinematics and statics analysis, the optimal design and workspace of the robot are analyzed with the positive cable tension constraint, which can guide the design of the cable-driven robot with a spring spine or other similar flexible bar with workspace requirements.

The remaining sections of this paper are organized as follows: in Section 2, we present the descriptions of the parallel robot including the notations used in this paper and the DOF parameterization for the mechanism. After that, the inverse position and statics are solved simultaneously in Section 3. Based on the statics, the optimal design for cable placements and the workspace of the robot is analyzed in Sections 4 and 5, respectively. Finally, conclusions are given in Section 6.

2. Configuration of the parallel robot

The proposed cable-driven parallel robot shown in Fig. 2 consists of four main components: a fixed base, a moving platform, three flexible cables with negligible mass and diameter, and a compression spine. The moving platform is driven by the cables and the connection points are $P_i (i = 1, 2, 3)$. The other end of each cable connects to a roller driven by a motor and the cables pass through the fixed base at points B_i. A coordinate frame *OXYZ* is attached to the fixed base, with the origin at the bottom center of the spring. The *Y*-axis is along OB_1, and the *Z*-axis is perpendicular to the base plane. A moving coordinate frame *pxyz* is attached to the moving platform, with its origin at the top center of the spring. The *y*-axis is along pP_1, and the *z*-axis is perpendicular to the moving platform plane. $\overrightarrow{OB_i}$ and $\overrightarrow{pP_i}$ are along the same direction in the initial configuration. Both B_i and P_i are equidistance to each other on the circle with radii $|OB_i| = a$ and $|pP_i| = b$ with respect to the center *O* and *p*, respectively. The coordinates of B_i in frame OXYZ are described as $B_1(0, a, 0), B_2(-\frac{\sqrt{3}}{2}a, -\frac{1}{2}a, 0), B_3(\frac{\sqrt{3}}{2}a, -\frac{1}{2}a, 0)$; the corresponding coordinates for other ends of the cables P_i in frame *pxyz* are $P_1(0, b, 0), P_2(-\frac{\sqrt{3}}{2}b, -\frac{1}{2}b, 0), P_3(\frac{\sqrt{3}}{2}b, -\frac{1}{2}b, 0)$. Denote the force value along the cable as t_i, the cable length between B_i and P_i as l_i, and the unit vector for the direction of force in each cable as ${}^{O}\mathrm{u}_i$. In the plane formed by *O*, *p* and *p′* with *p′* the projection of *p* to the fixed base, a planar body frame *Osh* is attached to the spring. The origin is the same as the frame *OXYZ*, the *h*-axis is the same as the *Z*-axis in frame *OXYZ* and the *s*-axis is along $\overrightarrow{Op'}$.

We assume the spring will bend in a plane. Moreover, since the torsional strength for the spring is quite large, we also assume the moving platform does not rotate about the *z*-axis of the body frame *pxyz*. In this case, we define four parameters to define the configuration of the moving platform, i.e., φ_s: angle between axis *s* and axis *X* (bending direction); φ_r: angle between the fixed base plane and the moving platform plane (bending amplitude); h_p: *h* coordinate for top center of the spring in frame *Osh* (vertical length of the bending spring); s_p: *s* coordinate for top center of the spring in frame *Osh* (lateral translation for the

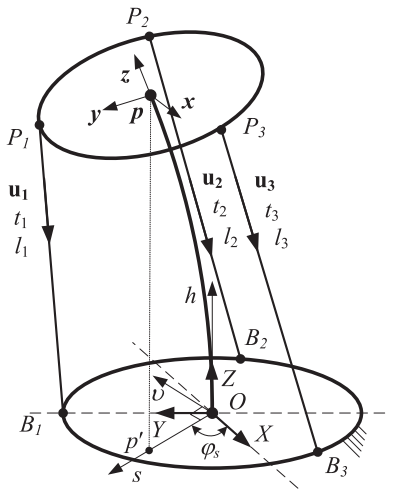

Fig. 2. Schematic of cable-driven and flexible parallel mechanism.

bending spring). However, only three of the four parameters are independent. Without loss of generality, we consider s_p to be the dependent parameter. In other words, s_p can be solved with given φ_s, φ_r, and h_p. This unspecified motion is frequently encountered in parallel manipulators [31]. Since the DOF for a mechanism is the number of independent coordinates needed to define its configuration [32], this mechanism has only three DOF.

Since φ_s and φ_r describe the orientation of the moving platform, we can get the rotational matrix from frame *pxyz* to *OXYZ* when φ_s and φ_r are given. Using the quaternion formulation, the rotational matrix can be obtained as:

$$ {}^{O}\mathbf{R}_p = \begin{bmatrix} t_{11} & t_{12} & t_{13} \\ t_{21} & t_{22} & t_{23} \\ t_{31} & t_{32} & t_{33} \end{bmatrix} \tag{1} $$

where

$$ \begin{aligned} &t_{11} = sin^2\varphi_s + cos\varphi_r cos^2\varphi_s, t_{12} = t_{21} = (cos\varphi_r - 1)cos\varphi_s sin\varphi_s, \\ &t_{13} = -t_{31} = sin\varphi_r cos\varphi_s, t_{23} = -t_{32} = sin\varphi_r sin\varphi_s, \\ &t_{22} = cos^2\varphi_s + cos\varphi_r sin^2\varphi_s, t_{33} = cos\varphi_r. \end{aligned} $$

Consequently, the homogeneous transformation matrix from frame *pxyz* to *OXYZ* can be obtained as:

$$ {}^{O}\mathbf{T}_p = \begin{bmatrix} {}^{O}\mathbf{R}_p & {}^{O}\mathbf{P}_p \\ 0 & 1 \end{bmatrix} \tag{2} $$

where ${}^{O}\mathbf{P}_p = [s_p cos\varphi_s, s_p sin\varphi_s, h_p]^{\mathrm{T}}$ is the position vector of point p in frame *OXYZ*.

3. Inverse kinematics and statics

The inverse position kinematics problem is stated as: given the desired moving platform posture $\mathbf{x} = [\varphi_s, \varphi_r, h_p]^{\mathrm{T}}$, we need to calculate the cable lengths l_i. The solution is straightforward by calculating $l_i = \left\| {}^{O}\mathbf{T}_p \overrightarrow{pP_i} - OB_i \right\|$ if s_p is solved from $\mathbf{x}$. However, s_p cannot be an arbitrary number. In fact, it is a characteristic of the spring lateral bending, which is caused by the forces acting on the spring. These forces come from the pulling forces in the three cables and the mass of the payload. Therefore, we should combine the inverse position and statics in order to obtain a solution.

We solve the problem in the following way. First of all, we transform all the cable forces to the equivalent force and torque applied at the spring's top center. Assume all the cable forces can be transformed into the bending plane *Osh*, we can convert all the forces to two perpendicular forces F_1 and F_2 in the plane, and a torque M perpendicular to the plane as shown in Fig. 3. Then, we combine the spring lateral bending equations and equilibrium equations of force and torque at the moving platform to solve s_p. Consequently, the inverse kinematics of the mechanism can be solved.

3.1. Static equations of the spring spine

The spring bending problem was first investigated by Timoshenko. He pointed out that the lateral bending of coil compression spring could be treated with the same methods as the elastic bars, but it was necessary to consider the change in length of the

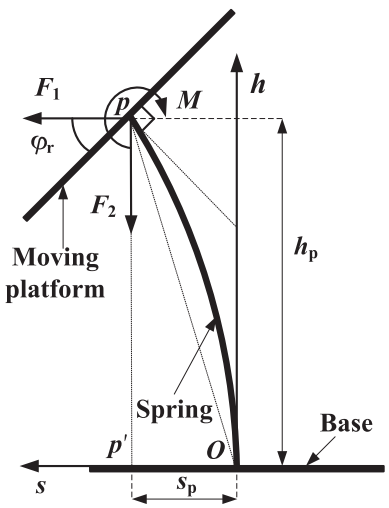

Fig. 3. Force and torque balance system.

spring due to compression since the change was not negligible as in the case of compressed bars [33]. Following this suggestion, the spring as shown in Fig. 3 will be bent by forces F_1 and F_2 plus a torque M. Since head bending angles are no more than 15° for healthy individuals in most time [34], we only consider the linear bending curve [33] in this paper. For any cross section of the spring, the linear equation with small bending is:

$$\beta\frac{d^2s}{dh^2} = M + F_2\left(s_p - s\right) + F_1\left(h_p - h\right) \tag{3}$$

with initial conditions for the built-in end connected to the fixed base and the free end connected to the moving platform

$$s(0) = 0, \quad s'(0) = 0, \quad s\left(h_p\right) = s_p, \quad s'\left(h_p\right) = tan\varphi_r \tag{4}$$

where $s' = ds/dh$.

Based on Eqs. (3) and (4), two equations regarding F_1 and M can be derived as a function of s_p [10]:

$$F_1 = D_1 s_p + E_1 \tag{5}$$

$$M = D_2 s_p + E_2 \tag{6}$$

where

$$\begin{aligned}
D_1 &= -\frac{a_2c_1 - a_1c_2}{a_2b_1 - a_1b_2},\\
E_1 &= -\frac{a_2d_1 - a_1d_2}{a_2b_1 - a_1b_2},\\
D_1 &= -\frac{b_2c_1 - b_1c_2}{a_1b_2 - a_2b_1},\\
E_2 &= -\frac{b_2d_1 - b_1d_2}{a_1b_2 - a_2b_1},\\
a_1 &= 1 - cos\left(\sqrt{F_2/\beta h_p}\right),\\
b_1 &= \sqrt{\beta/F_2}sin\left(\sqrt{F_2/\beta h_p}\right) - h_p cos\left(\sqrt{F_2/\beta h_p}\right),\\
c_1 &= -F_2 cos\left(\sqrt{F_2/\beta h_p}\right),\\
d_1 &= 0,\\
a_2 &= \sqrt{F_2/\beta}sin\left(\sqrt{F_2/\beta h_p}\right),\\
b_2 &= cos\left(\sqrt{F_2/\beta h_p}\right) + h_p\sqrt{F_2/\beta}sin\left(\sqrt{F_2/\beta h_p}\right) - 1,\\
c_2 &= F_2\sqrt{F_2/\beta}sin\left(\sqrt{F_2/\beta h_p}\right),\\
d_2 &= -F_2 tan\varphi_r,
\end{aligned}$$

and β is the flexural rigidity after compression of the spring which can be calculated based on the flexural rigidity of the spring β_0 and spring length (initial length l_0 and length after compression h_p):

$$\beta = \beta_0\frac{h_p}{l_0}$$

Note that we use h_p to approximate the compressed spring length in this paper. In fact, the compressed spring length equals to h_p only when no bending motion of the spring ($\theta_p = 0$). If $\theta_p \neq 0$, we can approximate the compressed spring length using h_p due to the small bending angles considered in this paper [1,35].Consequently, the variable F_2 can be approximated using Hooke's law:

$$F_2 = K\left(l_0 - h_p\right) \tag{7}$$

where K is the spring constant.

3.2. Force and torque equilibrium

In order to balance the resultant force and torque shown in Fig. force, all cables must be able to create tension forces to achieve the equilibrium of the moving platform. The mass of the moving platform is taken as a mass point at the spring's top center with quantity m. The equilibrium conditions for force and torque for the moving platform are as follows:

$$\sum_{i=1}^{3} \mathrm{t}_i + \mathrm{F} = 0 \tag{8}$$

$$\sum_{i=1}^{3} {}^{O}\mathbf{r}_i \times \mathbf{t}_i + \mathbf{M} = 0 \tag{9}$$

where $\mathbf{t}_i = t_i {}^{O}\mathbf{u}_i$ and ${}^{O}\mathbf{r}_i = {}^{O}\mathbf{R}_p \cdot \overrightarrow{pB_i}$, $\mathbf{F} = [-F_1 cos\varphi_s, -F_1 sin\varphi_s, F_2 - mg]^{\mathrm{T}}$, and $\mathbf{M} = [Msin\varphi_s, -Mcos\varphi_s, 0]^{\mathrm{T}}$.

In Eqs. (8) and (9), there are in total seven unknowns: t_1, t_2, t_3, F_1, F_2, M and s_p. According to compression and bending equations of the spring, the three unknown parameters F_1, F_2, and M have been obtained as Eqs. (5), (6), and (7). We will show that t_1 to t_3 can also be represented as functions of s_p.

Force balance Eq. (8) can be can be decomposed into three equations:

$$s_p cos\varphi_s\left(t_1' + t_2' + t_3'\right) + t_{12} b\left[t_1' - \frac{1}{2}\left(t_2' + t_3'\right)\right] + \left[\frac{\sqrt{3}}{2}a - \frac{\sqrt{3}}{2}bt_{11}\right]\left(t_2' - t_3'\right) = -F_1 cos\varphi_s \tag{10}$$

$$s_p sin\varphi_s\left(t_1' + t_2' + t_3'\right) - (a - t_{22} b)\left[t_1' - \frac{1}{2}\left(t_2' + t_3'\right)\right] - \frac{\sqrt{3}}{2}bt_{21}\left(t_2' - t_3'\right) = -F_1 sin\varphi_s \tag{11}$$

$$h_p\left(t_1' + t_2' + t_3'\right) + bt_{32}\left[t_1' - \frac{1}{2}\left(t_2' + t_3'\right)\right] - \frac{\sqrt{3}}{2}bt_{31}\left(t_2' - t_3'\right) = F_2' \tag{12}$$

where $t_i' = t_i / l_i$, $F_2{}' = F_2 - mg$. Rewrite the above three equations in matrix form:

$$\mathbf{CX} = \mathbf{F} \tag{13}$$

where $\mathbf{X} = [t_1', t_2', t_3']^{\mathrm{T}}$ and items of the 3×3 matrix $\mathbf{C}$ are:

$$\begin{aligned}
c_{11} &= s_p cos\varphi_s + bt_{12} \\
c_{12} &= \frac{\sqrt{3}}{2}a + s_p cos\varphi_s - \frac{\sqrt{3}}{2}bt_{11} - \frac{1}{2}bt_{12} \\
c_{13} &= -\frac{\sqrt{3}}{2}a + s_p cos\varphi_s + \frac{\sqrt{3}}{2}bt_{11} - \frac{1}{2}bt_{12} \\
c_{21} &= -a + s_p sin\varphi_s + bt_{22} \\
c_{22} &= \frac{1}{2}a + s_p sin\varphi_s - \frac{\sqrt{3}}{2}bt_{21} - \frac{1}{2}bt_{22} \\
c_{23} &= \frac{1}{2}a + s_p sin\varphi_s + \frac{\sqrt{3}}{2}bt_{21} - \frac{1}{2}bt_{22} \\
c_{31} &= h_p + bt_{32} \\
c_{32} &= h_p - \frac{\sqrt{3}}{2}bt_{31} - \frac{1}{2}bt_{32} \\
c_{33} &= h_p + \frac{\sqrt{3}}{2}bt_{31} - \frac{1}{2}bt_{32}
\end{aligned}$$

Provided matrix $\mathbf{C}$ is full rank, i.e., the determination of matrix $\mathbf{C}$ satisfies

$$det(\mathbf{C}) = \frac{3\sqrt{3}}{2}(a-b)\left(ah_p - bh_p cos\varphi_r - bs_p sin\varphi_r\right) \neq 0 \tag{14}$$

the linear Eq. (13) with respect to $\mathbf{X}$ has a unique solution

$$\begin{bmatrix} t_1' \\ t_2' \\ t_3' \end{bmatrix} = \mathbf{C}^{-1} \begin{bmatrix} -F_1 cos\varphi_s \\ -F_1 sin\varphi_s \\ F_2' \end{bmatrix} \tag{15}$$

Substituting the above three solutions into the first equation of torque balance Eq. (9) which can be rewritten as

$$\begin{aligned}
&\left(\frac{1}{2}h_p t_{22} - \frac{1}{2}s_p sin\varphi_s t_{32} - \frac{1}{4}at_{32}\right)\left(t_2' + t_3'\right) \\
&\quad + \left(\frac{\sqrt{3}}{2}h_p t_{21} - \frac{\sqrt{3}}{2}s_p sin\varphi_s t_{31} - \frac{\sqrt{3}}{4}at_{31}\right)\left(t_2' - t_3'\right) \\
&\quad + \left(s_p sin\varphi_s t_{32} - at_{32} - h_p t_{22}\right)t_1' = -\frac{M}{b}sin\varphi
\end{aligned} \tag{16}$$

and after some calculation, we have

$$\begin{aligned}&2bsin\varphi_s sin\varphi_r F_2^{'} s_p^2+\\&2b\left(sin\varphi_s sin\varphi_r h_p F_1+sin\varphi_s cos\varphi_r h_p F_2^{'}\right)s_p+\\&b\left(2sin\varphi_s sin\varphi_r M+asin\varphi_r cos2\varphi_s F_2^{'}\right)s_p+\\&b\left(2h_p^2 sin\varphi_s cos\varphi_r-absin\varphi_s sin^2\varphi_r+asin\varphi_r cos2\varphi_s h_p\right)F_1-\\&absin\varphi_r sin\varphi_s(a-bcos\varphi_r)F_2^{'}-2h_p sin\varphi_s(a-bcos\varphi_r)M=0\end{aligned} \tag{17}$$

Substituting Eqs. (5) and (6) into Eq. (17), the following equation is obtained:

$$As_p^2+Bs_p+C=0 \tag{18}$$

where

$$\begin{aligned}A &= 2bsin\varphi_r sin\varphi_s(F_2{}'+h_p D_1+D_2)\\B &= \left(2bh_p^2 cos\varphi_r sin\varphi_s-ab^2 sin^2\varphi_r sin\varphi_s+abh_p sin\varphi_r cos2\varphi_s\right)D_1\\&\quad -2h_p sin\varphi_s(a-bcos\varphi_r)D_2+2bh_p sin\varphi_s\left(F_2^{'}cos\varphi_r+E_1 sin\varphi_r\right)\\&\quad +bsin\varphi_r\left(2E_2 sin\varphi_s+aF_2^{'}cos2\varphi_s\right)\\C &= \left(2bh_p^2 cos\varphi_r sin\varphi_s-ab^2 sin^2\varphi_r sin\varphi_s+abh_p sin\varphi_r cos2\varphi_s\right)E_1\\&\quad -absin\varphi_r sin\varphi_s(a-bcos\varphi_r)F_2^{'}-2h_p sin\varphi_s(a-bcos\varphi_r)E_2\end{aligned}$$

Eq. (18) is a quadratic equation and A, B, C are known for given φ_r, φ_s and h_p. Then, s_p can be obtained by solving the Eq. (18). Once s_p is obtained, all the other unknowns can be calculated.

Note that eq. (17) is derived based on full rank condition Eq. (14) of matrix $\mathbf{C}$. If $det(\mathbf{C})=0$, there are infinitely many values for $t_1{}'$, $t_2{}'$, $t_3{}'$. One can choose the values of $t_1{}'$, $t_2{}'$, $t_3{}'$ to make them compatible to Eq. (16) and therefore compatible to Eq. (17). Additionally, $det(\mathbf{C})\neq 0$ can be explained as $a\neq b$ and $ah_p - bh_p cos\varphi_r - bs_p sin\varphi_r \neq 0$. For the latter one, it can be rewritten as

$$\frac{a}{b}\cdot\frac{h_p}{|Op|}\neq cos(\varphi_r-\beta) \tag{19}$$

where $\beta=\angle Opp'$ and $|Op|$ denotes the line distance as shown in Fig. 3. Based on the geometry in Fig. 3, one can see that condition Eq. (19) will be simplified to the same one $a\neq b$ when $\varphi_r=0$, which means no bending motion of the moving platform. In real bio-inspired robotic head developments [7,11], the constrain $a>b$ holds for mimicking real human neck anatomy and $h_p\approx|Op|$ holds because of small bending angles of human heads (no more than 15°) in daily life [34]. In other words, condition Eq. (19) will always hold in real robotic applications or simplify to $a\neq b$ when $\varphi_r=0$. As for the requirement $a\neq b$, it can be met easily in real applications. Furthermore, condition $a=b$ is apparently compatible to the smooth quadratic eq. (18) based on squeeze theorem. Intuitively, $a=b$ is not a singularity condition for the considered parallel mechanism which can be also proved by the numerical implementation in the following subsection.

One can see that the derivation and discussions on quadratic eq. (17) here differ from the one used in [10] for a similar mechanism with four driving cables. Moreover, the above discussion on conditions to achieve the quadratic equation here is more rigorous than the special case discussed in [10].

3.3. Simulations

The inverse position and statics analysis were simulated in MATLAB. Parameters of spring compression for the prototype are given as follows: the initial length $l_0=0.1016$m, the pitch $h_0=0.0195$m, the shearing modulus $G=81.2$ GPa, the elastic modulus $E=196.5$ GPa, the radius $r=0.0227$m, the diameter of the spring wire $d=0.00376$m, and the spring constant $K=4153$N/m. Therefore, the moment of inertia I of the cross-section of the spring wire and the flexural rigidity a_0 can be calculated as 9.811×10^{-12}m^4 and 0.2321, respectively. Radii of the cable connecting points are chosen as $a=b=0.05$m and the mass of the moving platform is $m=0.05$ kg. Inverse kinematics of the parallel robot is simulated with a fixed $h_p=0.085$m because in real applications h_p is only employed to adjust the pretension force in the three cables. By varying φ_r from 0 to $\pi/8$ and φ_s from 0 to 2π, the simulation results are shown in Fig. 4.

From Fig. 4, the following features can be observed: 1) the length and force complement each other for each cable. In other words, when the cable length is small, the force in the cable will be large. This feature is in accordance with intuition because when a cable exerts larger force on the moving platform, its length should be smaller. 2) when the bending amplitude of the moving platform φ_r is large, the variations of both the cable force and cable length are also large. The reason is that the more we want to bend the moving platform, the larger force is needed to act on it. 3) for a fixed bending amplitude φ_r, the curves of force and length curves for all the three cables with φ_s from 0 to 2π are symmetric.

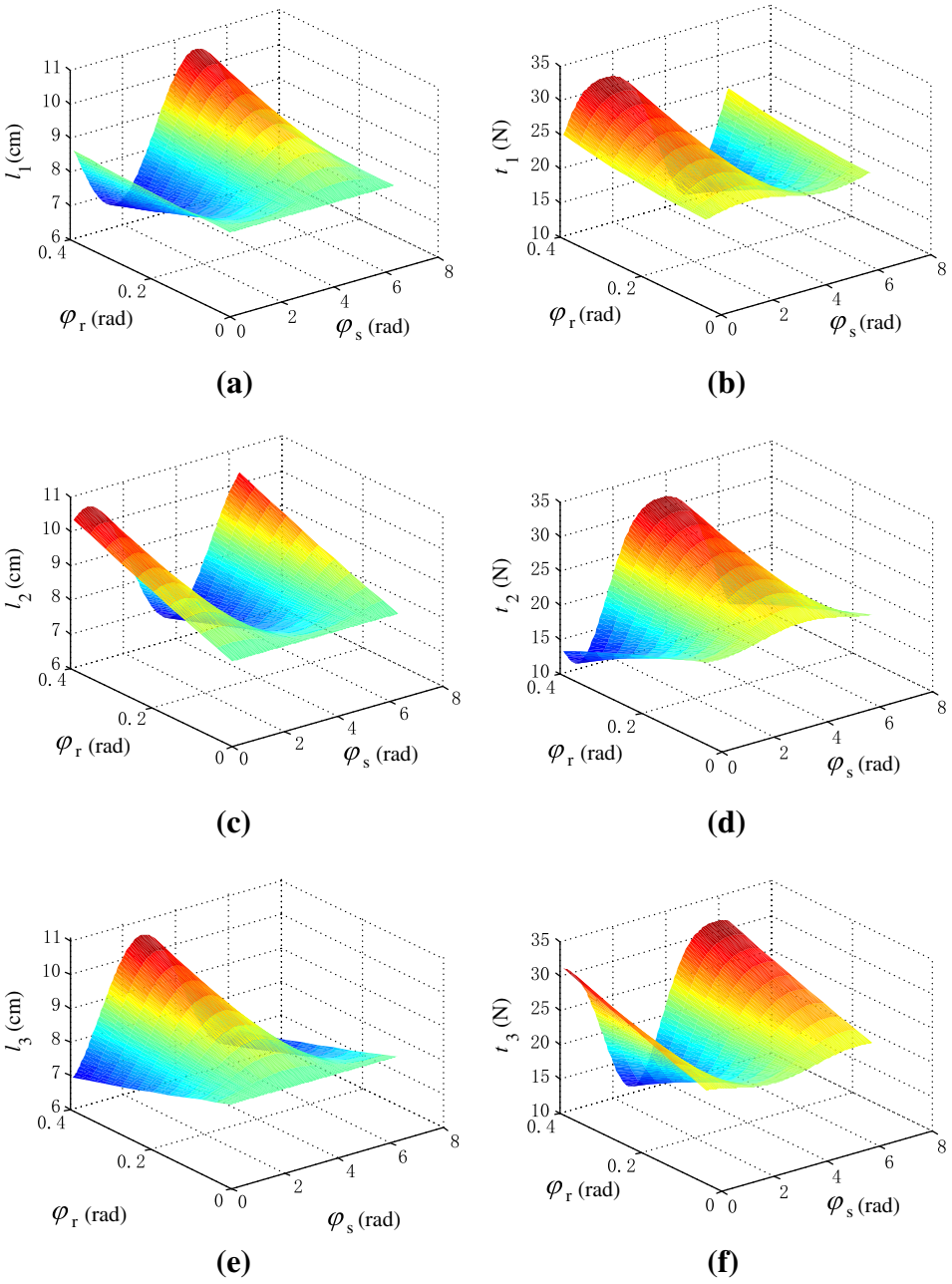

Fig. 4. Inverse position and statics illustration.

4. Optimal design

Based on the inverse kinematics analysis, in order to minimize actuation force to decrease the size of actuators and reduce energy consumption, we can optimize the parallel mechanism. Because all the variables should either be specified (φ_s, φ_r, and h_p) or solved (s_p, F_1, F_2, and M), the optimization variables come to be a and b, which represent the cables' end positions at the fixed base and moving platform. There are some researches on optimal tension force distribution among all the cables in cable-driven manipulators [30]. Some researchers also study how to choose the connecting point of the cables to optimize feasible workspace [36,37]. In the following, the numerical approach will be employed to obtain the optimal a and b to minimize actuation forces.

Let $\mathbf{t} = [t_1,\ t_2,\ t_3]^{\mathrm{T}}$ be the vector of all the cable forces. Two different vector norms will be used to define the measure:

- $2-\text{norm} : T_2 = \sqrt{\sum_{i=1}^{3} t_i^2}$
- $\infty - \text{norm} : T_\infty = max\{t_1,\ t_2,\ t_3\}$

Note that the cable forces are nonnegative because the unilateral actuation ability for cables. As a result, no absolute value symbols are needed in the above definition. In this paper, we will discuss the optimization based on the two measures, and we call them minimum average T and Min–Max T, respectively [31].

Since the type of measure is clear from the context, we will drop the subscript and use T to represent the above two norms. T is a function of φ_s, φ_r, h_p, a, and b. Without loss of generality, we fix the variable $h_p = 0.085\text{m}$ because different h_p can be obtained by pretightening all the three cables simultaneously. Now, we can write:

$$T = \lambda(\varphi_s, \varphi_r, a, b) \quad \lambda : \mathbb{R}^4 \rightarrow \mathbb{R}$$

Note that an analytical expression for T is available because expression for individual t_i can be obtained based on inverse kinematics. However, the final expression for T is very complicated. We will not try to use the analytical approach to derive the optimal solution; instead, we will use iterative numerical method.

Define a scalar function of only a and b as $\Phi(a, b)$, $\Phi : \mathbb{R}^2 \rightarrow \mathbb{R}$, then the minimization problem can be generally stated as:

$$\begin{array}{l} \text{minimize} \quad \Phi(a,b) \\ \text{subject to} \quad a_l \le a \le a_u, b_l \le b \le b_u \quad \text{and} \quad t_i \ge 0 (i = 1,2,3) \end{array}$$

where a_l, b_l, a_u, and b_u are the lower bound and upper bound for a and b, respectively, whose values are based on the size of human neck and the outer diameter of the spring. And $t_i \ge 0$ is the condition that the forces in cables cannot be negative. The optimal results can be expressed as:

$$\Phi^* = \Phi(a^*, b^*) = \min_{a,b}\{\Phi(a,b)\}$$

where * denotes the optimal values for both function and variables.

4.1. Minimum average T

In this case, we want to minimize the average T over the workspace W of the mechanism. The minimum average T objective function is defined as:

$$\Phi_{\text{ave}}(a,b) = \frac{1}{W}\int_W \lambda(\varphi_s, \varphi_r, a, b)\text{d}W$$

The reason we choose minimum average T as the above objective function is because it corresponds to the minimal overall "energy" consumption, especially for T_2, during continuous robotic head motion. And energy consumption is always an important index during robot development.

It is difficult to obtain the analytical expression for $\Phi_{ave}(a, b)$ because even the expression of t_i for each cable is rather complicated as discussed before. However, it is possible to use the numerical integration method, and the adaptive Simpson quadrature in MATLAB [38] is employed to obtain the double integral Φ_{ave}.

Since Φ_{ave} is a nonlinear function of a and b, we use the Quasi–Newton nonlinear optimization algorithm in MATLAB Optimization Toolbox [39] to minimize Φ_{ave}. During the optimization, the lower bound and upper bound of the a and b are selected as $a_l = b_l = 0.03\text{m}$ and $a_u = b_u = 0.08\text{m}$. As the algorithm doesn't guarantee the convergence to the global minima, we try different initial points to obtain the final result. Moreover, graphs are presented for $\Phi_{ave}(a, b)$ to check the optimization results.

The numerical optimization results for the minimum average T with different measures are shown in Table 1. From the table, we see that different initial points converge to the same optimal points with different converge steps for different measures; however, the optimized results of different measures are quite different. The three-dimensional graphs for $\Phi_{ave}(a, b)$ are shown in Fig. 5. From the figure, one can see that the values of a and b for the minimal measures are in accordance with the optimization results shown in Table 1. Although the optimal point for T_∞ is (0.0319, 0.0300), many non-optimal points have function value Φ_{max} closing to Φ^*_{max}, which can be seen from the large area with almost the same color, including the optimal point (0.0800, 0.0791) for T_2. Therefore, $(a^*, b^*) = (0.0800, 0.0791)$ can be chosen for future implementation if the minimal average value of T, i.e., the energy consumption, is the major concern.

Table 1
Optimization results for minimum average T.

Measure	(a, b)	Φ_{ave}	(a^*, b^*)	Φ^*_{ave}	Steps
T_2	(0.05, 0.06)	40.6912	(0.0800, 0.0791)	40.0658	9
T_2	(0.06, 0.05)	40.5278	(0.0800, 0.0791)	40.0658	8
T_∞	(0.05, 0.06)	23.1844	(0.0319, 0.0300)	22.9688	7
T_∞	(0.06, 0.05)	23.0899	(0.0319, 0.0300)	22.9688	6

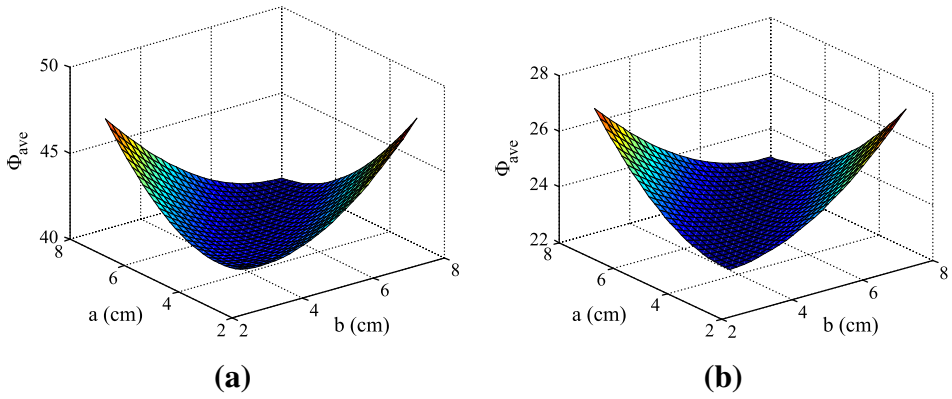

Fig. 5. Average T objective function Φ_{ave}: (a) T_2, (b) T_∞.

4.2. Min–Max T

The min–max objective is to minimize the maximum value for T over W. The function can be defined as:

$$\Phi_{max}(a,b) = \max_{W} \ \lambda(\varphi_s,\ \varphi_r,\ a,\ b)$$

We choose Min–Max T as the other objective function because it corresponds to the minimum "power" required for each driving motor, which determines the size of the motor in general. This objective function is more effective using the measure T_∞ than T_2. Reducing the actuator size is desirable during bio-inspired robots development.

Obtaining analytical expression for $\Phi_{max}(a, b)$ is also difficult. We discretize φ_s and φ_r and evaluate the value at the resulting points. With a dense discretization, the function value for $\Phi_{max}(a, b)$ can be approximated. The lower bound and upper bound of the a and b are also selected as $a_l = b_l = 0.03$m and $a_u = b_u = 0.08$m during the optimization.

The numerical optimization results for the Min–Max T with different measures are shown in Table 2. From the table, we can also see that different initial points converge to the same optimal results with same measure; moreover, the results for different measures are very close to each other. They also have different converge steps. The graphs for $\Phi_{max}(a, b)$ by discretizing a and b are shown in Fig. 6. From the figure,one can see that the optimal points shown in Table 2 are consistent with the figure. Therefore, $(a^*,\ b^*) = (0.0800,\ 0.0797)$ can be selected for future implementation if the minimal maximum value of T, i.e. the actuator size, is the major concern.

The optimal results based on the two objective functions and measures suggest that, with the same lower and upper bound for a and b, it's better to place all the cables near the upper bound to obtain minimum actuation force corresponding to either energy consumption or actuation size. Another observation from the optimal results is that the best solution has a radius ratio a/b close to one.

5. Workspace analysis

For a cable-driven parallel robot, its workspace is the space where sets of positive cable tensions exist because they are needed to constrain the moving platform all the time regardless of any external wrench [40]. The workspace of the mechanism in this paper is defined as the set of the center points of moving platform when all the cables are in tension. Assume the resulting wrench of the cables applied on the moving platform as $\mathbf{w}$, then $\mathbf{w} = -[\mathbf{F}, \mathbf{M}]^{\mathrm{T}}$, and Eq. (8), (9) can be rewritten as:

$$\begin{bmatrix} {}^{O}\mathbf{u}_1 & {}^{O}\mathbf{u}_2 & {}^{O}\mathbf{u}_3 \\ {}^{O}\mathbf{r}_1\times{}^{O}\mathbf{u}_1 & {}^{O}\mathbf{r}_2\times{}^{O}\mathbf{u}_2 & {}^{O}\mathbf{r}_3\times{}^{O}\mathbf{u}_3 \end{bmatrix} \begin{bmatrix} t_1 \\ t_2 \\ t_3 \end{bmatrix} = \mathbf{w} \tag{20}$$

Table 2
Optimization results for Min–Max T.

Measure	(a, b)	Φ_{max}	(a^*, b^*)	Φ^*_{max}	Steps
T_2	(0.05, 0.06)	43.2207	(0.0800, 0.0773)	41.9123	8
T_2	(0.06, 0.05)	42.7313	(0.0800, 0.0773)	41.9123	8
T_∞	(0.05, 0.06)	31.1679	(0.0800, 0.0797)	27.9727	6
T_∞	(0.06, 0.05)	30.8211	(0.0800, 0.0797)	27.9727	7

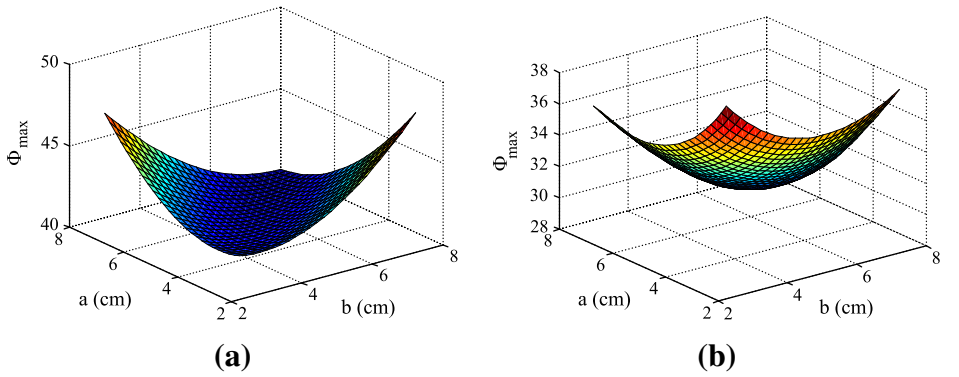

Fig. 6. Maximum T objective function Φ_{max}: (a) T_2, (b) T_∞.

Assume $\xi_i = [{}^{o}\mathbf{u}_i, {}^{o}\mathbf{r}_i \times {}^{o}\mathbf{u}_i]^T$ is defined as the line vector of the ith cable. The static equilibrium model in a compact form can be obtained:

$$\mathbf{At} = \mathbf{w} \tag{21}$$

where $\mathbf{A} = [\xi_1, \xi_2, \xi_3]$ and $\mathbf{t} = [t_1, t_2, t_3]^T$. $\mathbf{A}$ is called structure matrix, which is highly relied on the configuration of the mechanism and posture of the moving platform. $\mathbf{t}$ is the tension vector of the 3 cables.

If the moving platform is included within the workspace, the following conditions have to be satisfied:

$$\mathbf{At} = \mathbf{w}, \forall\ \mathbf{w}, \mathbf{t} > 0 \tag{22}$$

Condition (Eq. 22) is equivalent to the following conditions [41]:

$$\begin{cases} \text{Rank}(A) = 3 \\ \text{Null}(A) \cap \mathbb{R}_+^3 \neq \varnothing \end{cases} \tag{23}$$

where Null(A) is the null space of structure matrix $\mathbf{A}$, $\mathbb{R}_+^3$ is the positive set of 3 dimension real space, and $\varnothing$ is the empty set.

According to condition (Eq. 23), the procedure to identify whether a pose belonging to the translational workspace consists of the following four steps:

1. Fix the orientation of the moving platform.
2. Discretize a prescribed space into discrete points with a certain step. The structure matrix $\mathbf{A}$ and $\mathbf{t}$ are computed at each point.

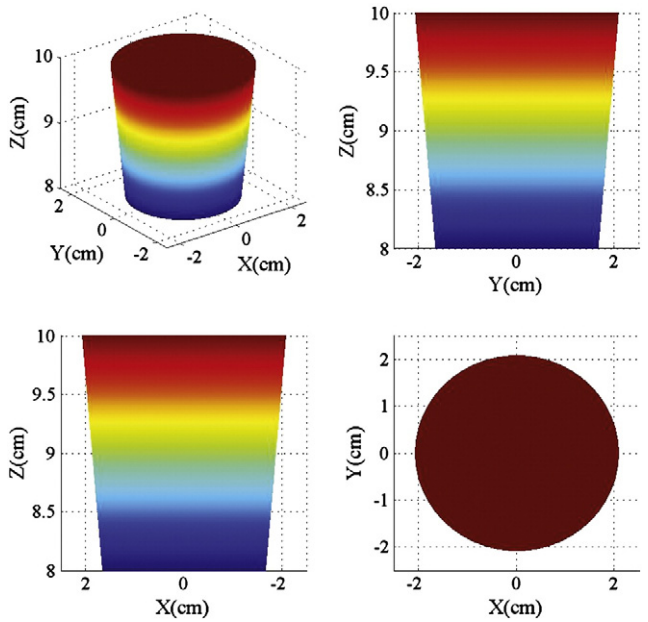

Fig. 7. The translational workspace with $\varphi_r = \pi/8$, $a = b = 0.05$ m.

3. Determine the rank of the structure matrix A and $\mathbf{t}$. If $\mathbf{A}$ is full rank and $\mathbf{t} > 0$, the point is included within the workspace, go to next step.
4. Record all the discrete points satisfying the step 3, and the space composed by these points is the translational workspace.

To illustrate the workspace analysis of the robot presented in this paper, numerical solutions are computed to show the characteristic of the robot. According to the method mentioned above, fix the angle $\varphi_r = \pi/8$, and discretize the rectangle space ($x \in [-0.03, 0.03]$, $y \in [-0.03, 0.03]$, $z \in [0.08, 0.1]$) at certain steps. Based on the above four steps, the Cartesian 3D space and 2D space of the robot with $a = b = 0.05$ m are drawn in Fig. 7. As shown in the figure, one see that the translational workspace is an inverted cone which conforms to the objective facts. In fact, the translational workspace varies with different values of a/b. Generally, the volume of the translational workspace of the robot will increase with the increase of value of a/b. The workspace of the robot with $a = 0.03$ m, $b = 0.08$ m and $a = 0.08$ m, $b = 0.03$ m are shown in Figs. 8 and 9, respectively. It can be seen clearly that the volume of the workspace with $a/b \approx 2.67$ is larger than the one with $a/b = 0.375$, and volume of the workspace with $a/b = 1$ is in between. In order to further verify this observation, we also give another workspace of robot when $a = 0.08$ m, $b = 0.0797$ m (which is the optimal value in Section 4) as shown in Fig. 10. We can see that the volumes of the workspace in Figs. 7 and 10 are essentially the same because the values of a/b are equal.

The workspace analysis results show that workspace volume tends to be higher with a larger radius ratio a/b. This conclusion contradicts the one yielded from the optimal design. These two conclusions leads to that proper values of a and b ($a > b$) could be selected by considering both the minimum actuation force and larger workspace volume. Anatomical structure of human neck does have $a/b > 1$ corresponding to the studied cable driven parallel mechanism which means, we believe, both minimum actuation force and larger workspace volume are taken into account. The reality could also prove the correctness of the performed optimal design and workspace analysis of the bio-inspired cable driven parallel robot.

6. Conclusions

This paper presents a bio-inspired flexible parallel robot whose moving platform and the base are connected with flexible supportive compression spring spine and three driving cables. Inverse kinematics, optimal design and workspace of the robot are analyzed and numerically implemented. Different from the underconstrained cable-driven parallel robots without flexible spines, the inverse kinematics has to be solved by combining the force and torque balance equations together with the lateral bending equations of the spring spine. This method can be applied to other parallel mechanisms with flexible spines. Based on the combined inverse position and statics analysis, optimal design for reducing actuation force with respect to place the three cables is performed. The optimization results show that it's better to place the cables near the upper bound. Subsequently, numerical implementations show that the translational workspace of the robot is an inverted cone and generally its volume will increase as the increase of value a/b (ratio between the connecting radii of the driving cables to the base and to the moving platform).

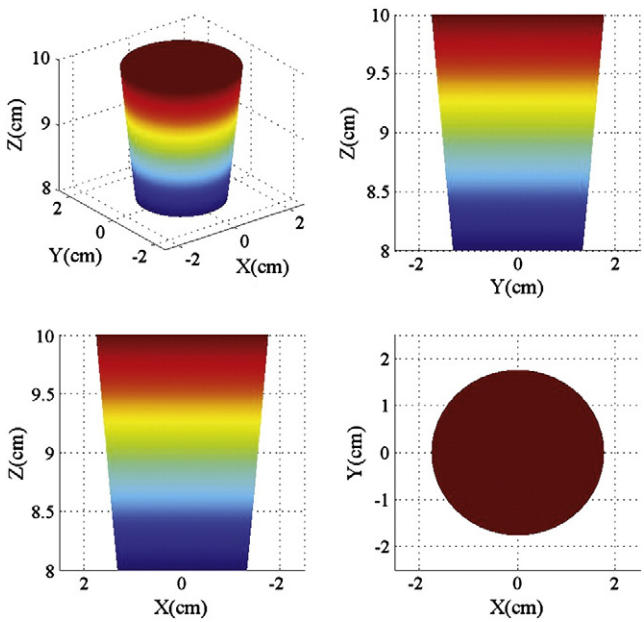

Fig. 8. The translational workspace with $\varphi_r = \pi/8$, $a = 0.03$ m, $b = 0.08$ m.

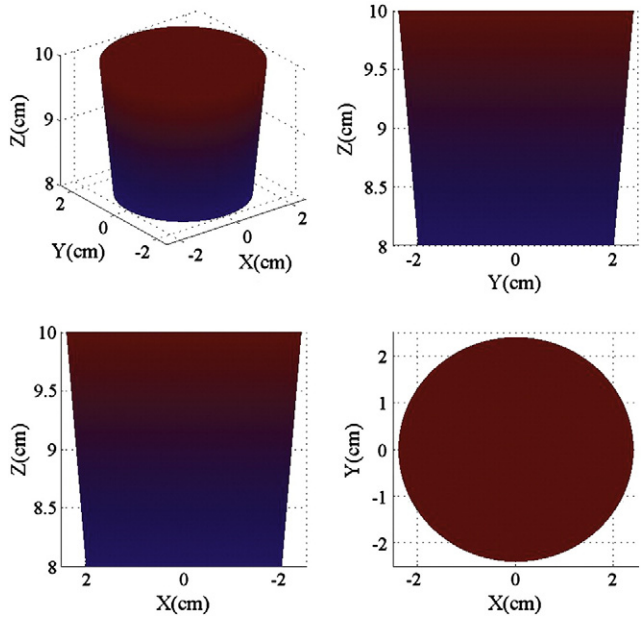

Fig. 9. The translational workspace with $\varphi_r = \pi/8$, $a = 0.08$ m, $b = 0.03$ m.

Therefore, taking both minimum actuation force and larger workspace into account to develop cable driven parallel robots with flexible spine, proper biomimetic values of a and b ($a > b$) should be followed.

Acknowledgment

The work is partially supported by National Science Foundation of China with No. 11102039, the Opening Fund of Jiangsu Key Laboratory of Remote Measurement and Control Technology with No. 7722009001, and the National Student Research Training Program of Southeast University with No. 1310286058.

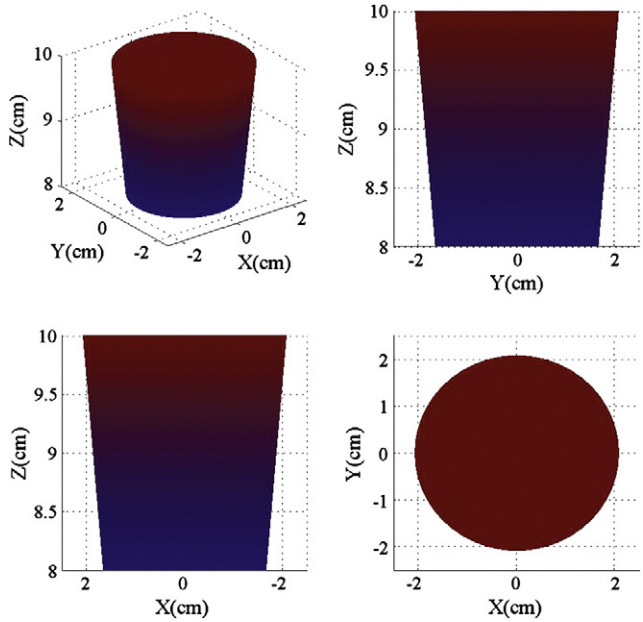

Fig. 10. The translational workspace with $\varphi_r = \pi/8$, $a = 0.08$ m, $b = 0.0797$ m.

References

[1] B. Gao, J. Xu, J. Zhao, N. Xi, Y. Shen, R. Yang, A humanoid neck system featuring low motion-noise, J. Intell. Robot. Syst. 67 (2012) 101–116.
[2] A.A. White, M.M. Panjabi, Clinical biomechanics of the spine, JB Lippincott, Philadelphian, 1990.
[3] Y. Sakagami, R. Watanabe, C. Aoyama, S. Matsunaga, N. Higaki, K. Fujimura, The intelligent ASIMO: system overview and integration, 2002, pp. 2478–2483.
[4] H. Hirukawa, F. Kanehiroa, K. Kanekoa, Humanoid robotics platforms developed in HRP, Robot. Auton. Syst. 48 (4) (2004) 165–175.
[5] J. Han, S. Zeng, K. Tham, M. Badgero, J. Weng, Dav: a humanoid robot platform for autonomous mental development, Proceedings of the 2nd International Conference on Development and Learning, Cambridge, Massachusetts, USA, 2002, pp. 73–81.
[6] I.-W. Park, J.-Y. Kim, B.-K. Cho, J.-H. Oh, Control hardware integration of a biped humanoid robot with an android head, Robot. Auton. Syst. 56 (1) (2008) 95–103.
[7] R. Beira, M. Lopes, M. Praca, Design of the robotcub (iCub) head, Proceedings of IEEE International Conference on Robotics and Automation, Orlando, USA, 2006, pp. 94–100.
[8] T. Asfour, P. Azad, N. Vahrenkamp, K. Regenstein, A. Bierbaum, K. Welke, J. Schroder, R. Dillmann, Toward humanoid manipulation in human-centred environments, Robot. Auton. Syst. 56 (1) (2008) 54–65.
[9] G. Carbone, H.-O. Lim, A. Takanishi, M. Ceccarelli, Stiffness analysis of biped humanoid robot WABIANRIV, Mech. Mach. Theory 41 (1) (2006) 17–40.
[10] B. Gao, J. Xu, J. Zhao, N. Xi, Combined inverse kinematic and static analysis and optimal design of a cable-driven mechanism with a spring spine, Adv. Robot. 26 (2012) 923–946.
[11] T. Hashimoto, S. Hitramatsu, T. Tsuji, H. Kobayashi, Development of the race robot SAYA for rich facial expressions, Proceedings of SICE-ICASE International Joint Conference, Bexco, Busan, Korea, 2006, pp. 5423–5428.
[12] F. Nori, L. Jamone, G. Metta, G. Sandini, Accurate control of a human-like tendon-driven neck, Proceedings of IEEE International Conference on Humanoid Robots, Pittsburgh, Pennsylvania, USA, 2007, pp. 371–378.
[13] L. Jamone, M. Fumagalli, G. Metta, Machine learning based control of a human-like tendon-driven neck, Proceedings of IEEE International Conference on Robotics and Automation, Anchorage, AK, USA, 2010, pp. 859–865.
[14] H. Su, L. Dickstein-Fischer, K. Harrington, Cable driven elastic parallel humanoid head with face tracking for autism spectrum disorder interventions, Proceedings of the IEEE Engineering International Conference on Medicine and Biology Society, Buenos Aires, Argentina, 2010, pp. 467–470.
[15] I. Toshima, S. Aoki, T. Hirahara, An acoustical tele-presence robot: TeleHead II, Proceedings of IEEE/RSJ International Conference on Intelligent Robots and Systems, Sendai, Japan, 2004, pp. 2105–2110.
[16] H. Kawano, H. Ando, T. Hirahara, C. Yun, S. Ueha, Application of a MDOF ultrasonic servomotor in an auditory tele-existence robot, IEEE Trans. Robot. 21 (2005) 790–800.
[17] S. Behzadipour, A. Khajepour, Cable-based robot manipulators with translational degrees of freedom, in: S. Cubero (Ed.), Industrial Robotics: Theory, Modeling and Control, Pro Literatur Verlag, 2006, pp. 211–236.
[18] P. Bosscher, I. Ebert-Uphoff, A stability measure for underconstrained cable-driven robots, Proceedings of IEEE International Conference on Robotics and Automation, New Orleans, USA, 2004, pp. 4943–4949.
[19] M. Carricato, J-P. Merlet, Stability analysis of underconstrained cable-driven parallel robots, IEEE Trans. Robot. 29 (2013) 288–296.
[20] G. Abbasnejad, M. Carricato, Real solutions of the direct geometrico-static problem of under-constrained cable-driven parallel robots with 3 cables: a numerical investigation, Meccanica 47 (2012) 1761–1773.
[21] J. Albus, R. Bostelman, N. Dagalakis, The NIST robotcrane, J. Robot. Syst. 10 (1993) 709–724.
[22] K. Maeda, S. Tadokoro, T. Takamori, On design of a redundant wire-driven parallel robot warp manipulator, Proceedings of IEEE International Conference on Robotics and Automation, Detroit, MI, USA, 1999, pp. 895–900.
[23] B. Zi, B.Y. Duan, J.L. Du, H. Bao, Dynamic modeling and active control of a cable-suspended parallel robot, Mechatronics 18 (2008) 1–12.
[24] P.H. Borgstrom, N.P. Borgstrom, M.J. Stealey, B. Jordan, G.S. Sukhatme, M.A. Batalin, W.J. Kaiser, Design and implementation of NIMS3D, a 3-D cabled robot for actuated sensing applications, IEEE Trans. Robot. 25 (2009) 325–339.
[25] N. Iwatsuki, T. Onoe, Motion control of wire-driven flexible link mechanism keeping stiffness against load, Proceedings of International on Mechatronics Technology, Osaka, Japan, 2010, pp. 395–398.
[26] S. Lahouar, E. Ottaviano, S. Zeghoul, Collision free path-planning for cable-driven parallel robots, Robot. Auton. Syst. 57 (2009) 1083–1093.
[27] B. Zi, X. Wu, J. Lin, Inverse kinematics and singularity analysis for a 3-DOF hybrid-driven cable-suspended parallel robot, Int. J. Adv. Robot. Syst. 9 (2012) 133–142.
[28] C. Pham, S. Yeo, G. Yang, M. Kurbanhusen, I. Chen, Force-closure workspace analysis of cable-driven parallel mechanisms, Mech. Mach. Theory 41 (2006) 53–69.
[29] M. Gouttefarde, C.M. Gosselin, Analysis of the wrench-closure workspace of planar parallel cable-driven mechanisms, IEEE Trans. Robot. 22 (2006) 434–445.
[30] M. Hassan, A. Khajepour, Optimization of actuator forces in cable-based parallel manipulators using convex analysis, IEEE Trans. Robot. 24 (2008) 736–740.
[31] J.A. Carretero, R.P. Podhorodeski, M.A. Nahon, C.M. Gosselin, Kinematic analysis and optimization of a new three degree-of freedom spatial parallel manipulator, ASME J. Mech. Des. 122 (2000) 17–24.
[32] G. Gogu, Mobility of mechanisms: a critical review, Mech. Mach. Theory 40 (2005) 1068–1097.
[33] S. Timoshenko, Theory of elastic stability, McGraw-Hill, New York, 1936.
[34] A.C. Sterling, D.G. Cobian, P.A. Anderson, B.C. Heiderscheit, Annual frequency and magnitude of neck motion in healthy individuals, Spine 33 (2008) 1882–1888.
[35] B. Gao, N. Xi, Y. Shen, J. Zhao, R. Yang, Development of a low motion-noise humanoid neck: statics analysis and experimental validation, Proceedings of IEEE International Conference on Robotics and Automation, Anchorage, AK, USA, 2010, pp. 1203–1208.
[36] C. Pham, S. Yeo, G. Yang, Workspace analysis and optimal design of cable-driven planar parallel manipulators, Proceedings of IEEE International Conference on Robotics and Automation, Singapore, 2004, pp. 219–224.
[37] J. Pusey, A. Fattah, S. Agrawal, E. Messina, Design and workspace analysis of *a* 6-6 cable-suspended parallel robot, Mech. Mach. Theory 39 (2004) 761–778.
[38] W. Gander, W. Gautschi, Adaptive quadrature — revisited, BIT, Numer. Math. 40 (2000) 84–101.
[39] MATLAB, Optimization toolbox user's guide, version 5.0, MathWorks, Natick, MA, 2010.
[40] Y. Zhang, X. Dai, Yang Yi, Workspace analysis of a novel 6-dof cable-driven parallel robot, IEEE International Conference on Robotics and Biomimetic, 2009, pp. 2403–2408.
[41] R. Verhoeven, Analysis of the workspace of tendon-based Stewart platforms, (Ph.D. dissertation) Duisburg-Essen University, Duisburg, 2004.